ACS APPLIED OPTICAL MATERIALS

pubs.acs.org/acsaom Article

Maximum Chirality Empowered by a Bound State in a Continuum in a Plasmonic Metasurface

Hanan Ali,* Simone Zanotti, Giovanni Pellegrini, Emilija Petronijevic, and Lucio Claudio Andreani

Cite This: ACS Appl. Opt. Mater. 2024, 2, 825−833 Read Online

ACCESS | Metrics & More | Article Recommendations

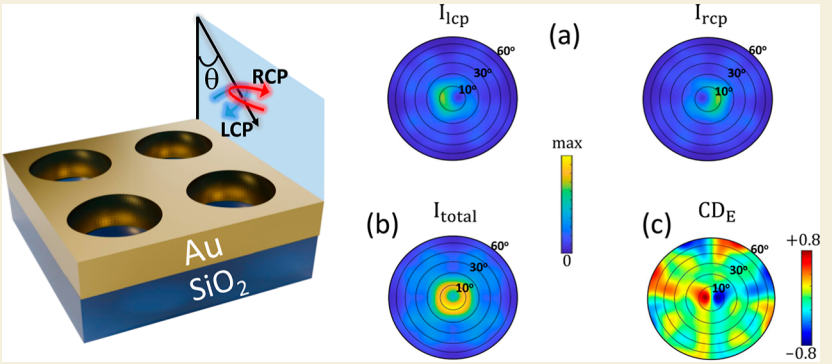

ABSTRACT: Achieving a strong and robust chiral response in plasmonic metasurfaces is among the key goals of current nanophotonic research. In this work, we theoretically show that the circular dichroism (CD) of a metal metasurface can be maximized by exploiting the concept of a bound state in a continuum (BIC) with symmetry breaking. We consider a gold metasurface with a deformation of circular holes into oval holes. The chiral response at small values of the angle of incidence is dominated by a quasi-BIC, with nearly maximal values of the absorption CD that are almost independent of the deformation. A strong CD in emission is also demonstrated. Symmetry analysis and mode profiles show that the extrinsically chiral response does indeed follow from a symmetry-broken BIC and is associated with a strong enhancement of the local electrical field. The concept of a plasmonic BIC with symmetry breaking provides a robust pathway to increase the chiral response in metal metasurfaces and opens research opportunities in chiral plasmonics that combine narrow resonances with local field enhancement.

KEYWORDS: *plasmonic metasurfaces, bound states in a continuum, symmetry breaking, extrinsic chirality, circular dichroism*

1. INTRODUCTION

Plasmonic metasurfaces with a periodic arrangement of nanoholes embedded in a metal film have attracted considerable attention in the past 25 years due to their ability to exhibit extraordinary transmission (EOT) of light.[1,2] This phenomenon arises from the resonant coupling between the electromagnetic field and surface plasmon polaritons (SPP) at the interfaces between the metal layer and the surrounding dielectric media.[3−5] The resonant enhancement of the electromagnetic field, driven by SPP excitations, forms the essence of EOT and gives rise to various distinctive phenomena. In this context, plasmonic metasurfaces are of extreme significance for unraveling fundamental aspects of light−matter interaction, and likewise in several technological applications such as surface-enhanced sensing.[6−11]

Our focus here is directed toward extrinsic chiral effects in plasmonic nanostructures. Chirality, defined by the absence of any symmetry plane, is a ubiquitous phenomenon observed both in the macro-world and at the nanoscale.[12] Chirality is particularly noteworthy in molecular and biological systems,[13] and plays a pivotal role in the field of drug sciences.[14] It is associated with distinct responses to incident circularly polarized light (CPL) with either right or left circular polarization (rcp, lcp). This gives rise to a circular dichroism (CD) signature in optical quantities, such as absorption, transmission, and luminescence. The plasmonic effect further enhances these properties, as widely discussed in the literature.[15−24] The chiral response can be intrinsic if the investigated structure lacks any plane of symmetry, usually by means of plasmonic nanostructures with chiral shapes.[17,25−27] Moreover, extrinsic chirality can occur in nonchiral geometries when probed at oblique incidence along a nonsymmetry

Received: February 29, 2024
Revised: April 8, 2024
Accepted: April 12, 2024
Published: April 25, 2024

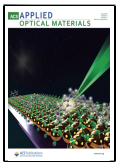

direction.[28−32] However, since chiroptical effects are often very weak, maximizing the chiral response (especially in lossy systems) often requires detailed optimization and the fabrication of complex structures. In view of future chiroptical applications, it is of great importance to identify simple geometries and general design criteria that can maximize the chiral response.

In dielectric systems, bound states in a continuum (BICs)—namely solutions of the wave equation that are resonant with the continuum but uncoupled to far-field radiation—have become a key concept that allows to achieve resonances with an ultrahigh Q-factor and to tailor light−matter interaction in many peculiar ways.[33−36] BICs have been shown to possess intriguing topological properties, as they are the center of polarization vortices with a quantized topological charge,[37] and can generate circularly polarized states upon symmetry breaking.[38,39] Numerous pioneering studies have reported on the generation of chiral quasi-BIC resonances with giant CD in dielectric systems.[40−46]

Metallic structures are usually dominated by a spectrally broad, low-Q response associated with SPPs, so that the identification and tailoring of BICs is hard to perform. Indeed, investigations of BICs in plasmonic systems have only recently started.[47−58] A common theme of these works is the trade-off between high Q-factor and strong field enhancement, which are difficult to optimize simultaneously. Using plasmonic BICs to increase the chiral response is considered in ref 53 for the THz region, with nearly spin-selective perfect absorption, and in ref 57 for the mid-infrared region, where quasi-BIC resonances with high Q ($\simeq$938) and strong CD ($\simeq$0.67) are demonstrated. In ref 58, resonance with a plasmonic BIC is employed to increase chiral second-harmonic generation. Nonetheless, plasmonic BIC in metal nanohole arrays and their possible role in increasing the chiral response are still to be investigated.

In the present work, we show that a gold metasurface with a periodic nanohole array can support a plasmonic BIC in the near-infrared region and that such a BIC can be exploited to maximize extrinsic chirality in the optical response. The crucial step leading to maximum chirality is to reduce the symmetry by deforming the nanoholes from a circular to an oval shape. Upon this symmetry breaking, absorption spectra display a quasi-BIC resonance on the low-energy side of the usual SPP peak, and such a peak dominates the chiral response at small angles of incidence. Values of the CD close to unity are demonstrated, which are almost independent of the deformation and are manifest in both absorption and emission CD. Analysis of mode profiles confirms the BIC nature of the resonance and highlights a strong enhancement of the local electric field, which is linked to the chiral response. The results suggest that a plasmonic BIC with symmetry breaking is a very useful concept to achieve a strong and robust CD in metallic metasurfaces. The combination of maximum chiral response, narrow resonance, and high local field enhancement widens the scope of metallic nanostructures for a number of fundamental studies in chiral photonics and for possible applications to advanced polarization-sensitive devices.

The rest of this article is organized as follows. In Section 2 we describe the investigated structure and the simulation methods. In Section 3 we present the results for absorption and emission CD related to a symmetry-broken BIC. Section 4 is devoted to a symmetry analysis of BIC and SPP mode profiles and to a discussion of field enhancement at resonances. Section 5 summarizes the main results, highlights the analogy with BICs in dielectric structures, and gives a discussion of open questions and new research avenues that spawn out of this work.

2. STRUCTURE AND METHODS

In the sketches of Figure 1a,b, we show the metasurface with the nanohole array (NHA) used in our study. A gold layer of thickness t = 100 nm is embedded between SiO_2 and air, as shown in the 3D view (a). A square lattice of period a = 500 nm, consisting of oval air holes, is etched in the metal layer. Each hole is made of two semiellipses, whose common semiaxis is denoted by r_1, while the differing semiaxes are denoted by r_2 and r_3, as in the 2D view (b). Obviously, the holes are circular when $r_1 = r_2 = r_3$. The values of t and a are fixed throughout this paper, and also, r_1 is fixed to 200 nm. The nanostructure is excited from the top (air side) with right- or left-circularly polarized light (CPL) under normal and oblique incidence. In the latter case, light is incident along the direction of the common axis of the semiellipses, i.e., in the xz plane.

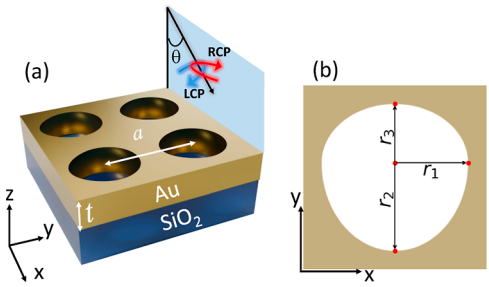

Figure 1. Sketch of the metasurface studied in this work. (a) 3D view: a layer of gold (thickness t = 100 nm) on a glass substrate is etched with a square lattice of air holes (lattice constant a = 500 nm). (b) 2D view of the unit cell: each hole has an oval shape consisting of two semiellipses with a common semiaxis r_1 and differing semiaxes r_2, r_3.

The optical properties of the oval nanohole array are numerically investigated by using two approaches. To calculate the absorption spectra and related CD maps, we apply the Bloch-mode scattering matrix method in the open-source software EMUstack, where a finite element approach is used to calculate the Bloch-modes in each 2D layer of the structure, and the electromagnetic field is propagated using a scattering matrix.[59,60] To calculate the field profiles, we employ the 3D finite difference time domain (FDTD) method using a Lumerical-Ansys commercial simulator. We set perfectly matched layers (PML) in the z-direction, and in order to perform calculations at a finite angle of incidence, we use the broadband fixed angle source technique.[61] The two methods generally yield results for the resonant energies that agree better than <0.01 eV. The dielectric functions of Au and SiO_2 are from the Lumerical database, taken from ref 62. Both mentioned methods allow the calculation of transmittance (T), reflectance (R), absorbance (A), and field profiles. We concentrate on the CD in absorption, which is defined as usual in terms of absorbance for left- or right-circular polarization (lcp, rcp) as

$$\mathrm{CD_A} = \frac{A_{\mathrm{lcp}} - A_{\mathrm{rcp}}}{A_{\mathrm{lcp}} + A_{\mathrm{rcp}}} \quad (1)$$

We also calculate emission spectra from a homogeneous layer of dipoles in FDTD by using a supercell technique and resolving the polarization of the emission in the far field projections, as described in ref 32. In this approach, the FDTD domain is surrounded by PMLs in all directions, encompassing 81 nanoholes. A single dipole is randomly oriented at a height of 10 nm below the Au layer, while its xy coordinates vary across one unit cell in 9 positions. The far-field emission is resolved in left- and right-CPL, and the averaging is done

https://doi.org/10.1021/acsaom.4c00097
ACS Appl. Opt. Mater. 2024, 2, 825−833

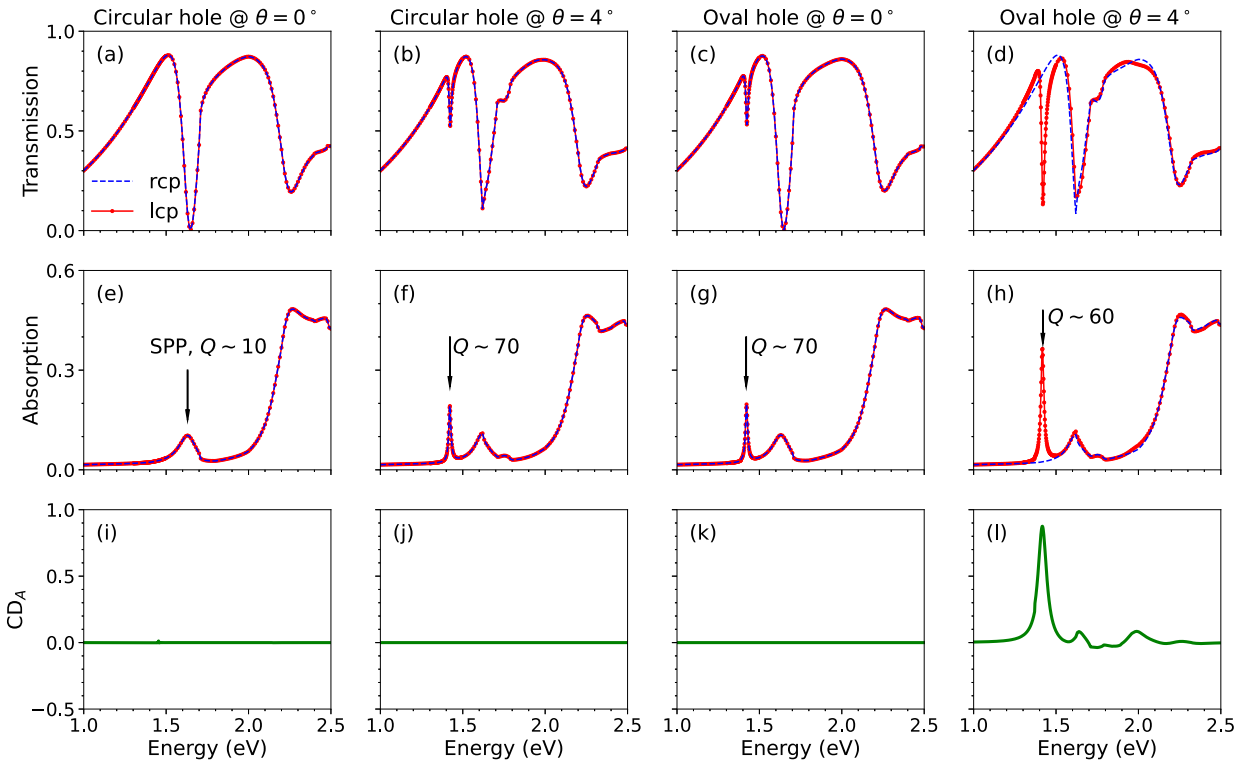

Figure 2. (a–d) Transmission and (e–h) absorption for right- and left circularly polarized light; (i–l) related CD in absorption. The spectra are calculated for four cases: circular holes with $r_1 = r_2 = r_3 = 200$ nm at normal incidence (first column) and at $\theta = 4°$ along the x orientation (second column), oval holes with $r_1 = 200$ nm, $r_2 = 240$ nm, $r_3 = 160$ nm at normal incidence (third column), and at $\theta = 4°$ along the x orientation (fourth column). The maximum CD in (l) is 0.874 at $E = 1.42$ eV.

over a random dipole orientation and xy positions. The average intensities I_{lcp} and I_{rcp} lead to a CD in the emission, defined as

$$CD_E = \frac{I_{lcp} - I_{rcp}}{I_{lcp} + I_{rcp}} \quad (2)$$

Since the oval holes have a mirror plane that is also a symmetry plane of the square lattice, the metasurface is invariant under reflection in the yz plane and is, therefore, nonchiral. Thus, no CD is expected at a normal incidence (no intrinsic chirality). However, for oblique incidence along any plane different from yz, the metasurface should display extrinsic chirality, and a CD is expected.[17,63,64] The effect is maximum for incidence along the xz direction.

3. DEFORMATION OF A CIRCULAR NANOHOLE LEADING TO A STRONG CD

In this section, we investigate the extrinsic chiral response of the metasurface upon the deformation of a circular hole. In Figure 2, we show transmission and absorption for left- and right-CPL as well as CD spectra, starting from a circular hole ($r_1 = r_2 = r_3 = 200$ nm) either at normal incidence or at oblique incidence ($\theta = 4°$ in the xz plane) and deforming it to an oval hole ($r_1 = 200$ nm, $r_2 = 240$ nm, and $r_3 = 160$ nm), again at normal incidence or at $\theta = 4°$ in the xz plane. For circular holes at normal incidence, the transmission spectra in Figure 2a display a broad extraordinary optical transmission (EOT) peak[1,2] that is interrupted by a dip around an energy $E \approx 1.640$ eV. The dip originates from the excitation of the surface plasmon polariton (SPP) related to the Au/SiO_2 interface.[3,5] Indeed, the absorption spectrum in Figure 2e shows a well-defined peak at $E = 1.63$ eV (≈760 nm) that corresponds to the energy of the Au/SiO_2 SPP folded at the Γ point of the first Brillouin zone of the square lattice[24] (the wavelength is close to $\lambda \simeq na$, where $n \simeq 1.45$ is the SiO_2 refractive index). This peak has a Q of ≈10, which is a typical Q-factor for plasmonic resonances. The energy region above 2 eV is uninteresting, as absorption is dominated by interband transitions in Au. The spectra are the same for left- and right-circular polarizations; thus, no CD occurs in Figure 2i.

For the case of circular holes at $\theta = 4°$ or of oval holes at normal incidence (Figure 2b,c), another transmission dip appears on the lower energy side of the SPP dip. Indeed, the absorption spectra in Figure 2f,g show a narrow peak at 1.42 eV (≈873 nm) with $Q \approx 70$ in addition to the SPP peak. Again, optical spectra are identical for right and left CPL; thus, no CD is observed in Figure 2j,k. Instead, for oval holes at oblique incidence (Figure 2d), the narrow dip on the low energy side becomes very strong for left CPL, while it disappears for right CPL. Similarly, the absorption peak in Figure 2h at 1.42 eV ($Q \approx 60$) is present only for left CPL. This points to a selective coupling of the incident field to a resonant mode that is fully left circularly polarized. Finally, Figure 2l shows that absorption CD occurs at oblique incidence along the x orientation, thus confirming the extrinsic chiral behavior of the metasurface under study. Most interestingly, absorption CD reaches a very high value of $CD_A = 0.874$ at $E = 1.42$ eV. As we show below, this strong and nearly optimal CD is intimately related to the nature of the resonance induced by the mechanism of symmetry breaking.

To analyze the effect of symmetry breaking, we further report on the dependence of CD on the incidence angle θ and on the deformation D, defined as

$$D = (r_2 - r_3)/(2r_1) \quad (3)$$

https://doi.org/10.1021/acsaom.4c00097
ACS Appl. Opt. Mater. 2024, 2, 825–833

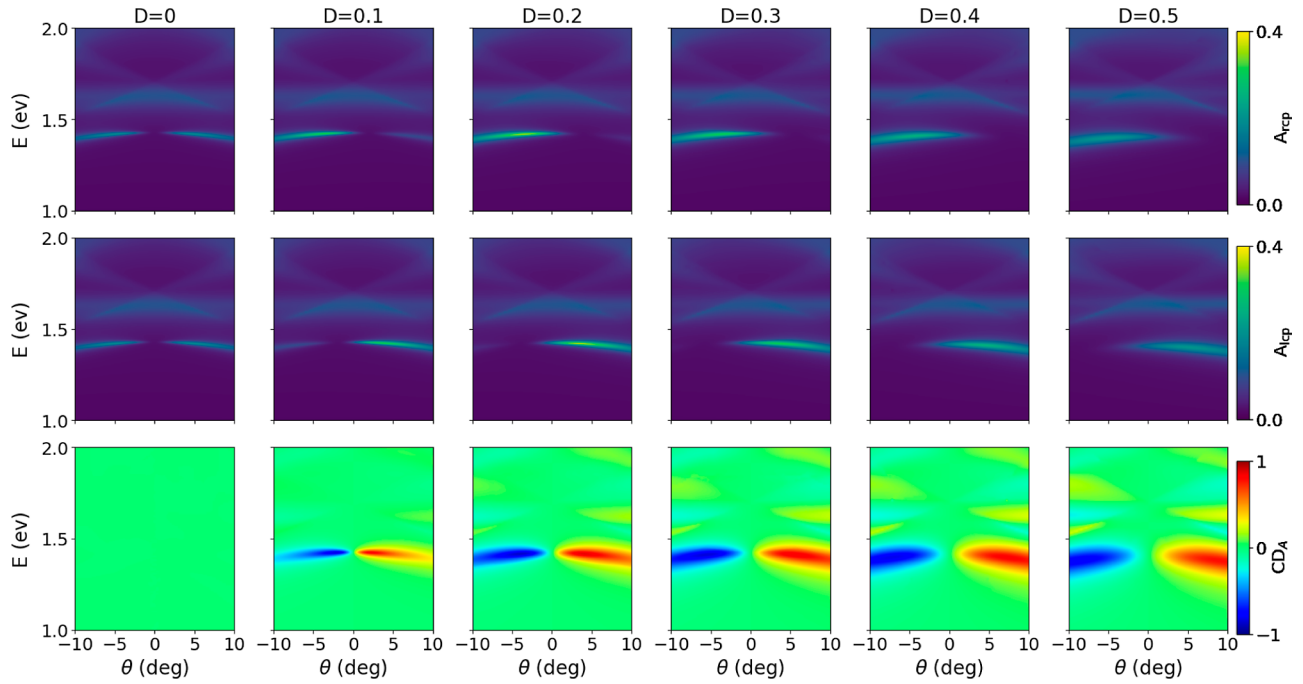

Figure 3. Absorption maps for right (upper panels) and left CPL (middle panels), as well as related CD maps (lower panels). The panels in each column are calculated for a given deformation $D = (r_2 - r_3)/(2r_1)$, for a common semiaxis $r_1 = 200$ nm and keeping $r_2 + r_3 = 2r_1$, as a function of angles θ for incidence along the x orientation.

We keep a fixed $r_1 = 200$ nm and vary the semiaxes r_2, r_3 in such a way that $r_2 + r_3 = 2r_1 =$ constant, so that the area of the nanoholes is kept fixed. In Figure 3, we show absorption maps for right- and left-CPL, as well as CD maps, for holes with a deformation D ranging from 0 to 0.5 (i.e., the last column corresponds to $r_2 = 300$ nm, $r_3 = 100$ nm) and for incidence angles θ from -10 to $10°$. For circular holes ($D = 0$), the absorption maps are identical for right- and left-CPL with no CD. The SPP peak around $\simeq$1.63 eV is weakly visible for all incidence angles, while a stronger peak at lower energy $\simeq$1.42 eV is visible for finite angles and becomes vanishingly weak at normal incidence. This is the behavior that is expected for a symmetry-protected BIC, and it leads us to identify the lower energy peak as being due to the excitation of a quasi-BIC (q-BIC) mode that becomes a BIC for circular holes at normal incidence. This identification will be further examined from the point of view of eigenmode symmetry in the next Section. In the following, for the sake of brevity, we shall refer to this peak as the "q-BIC peak". For any finite deformation, the q-BIC peak becomes asymmetric in θ: it is predominantly left circularly polarized for $\theta > 0$, while it is predominantly right circularly polarized for $\theta < 0$. The CD maps in the lower row clearly show the consequence of this asymmetry, as $CD(-\theta) = -CD(\theta)$: this is consistent with the presence of a yz symmetry plane, and it shows that the same metasurface structure can give CD of opposite behavior. The maximum CD for each deformation occurs at small angles θ that increase with the deformation. The absolute maximum $CD_A = 0.874$ occurs close to $\theta = 4°$ for a deformation $D = 0.2$ at $E = 1.42$ eV, i.e., the same parameters of Figure 2, (fourth column).

To better understand the relation between CD, incidence angle θ, and deformation D, we summarize our findings in Figure 4, where we present the results for maximum CD and optimal θ as a function of the deformation. The maximum CD occurs for the q-BIC peak around $E = 1.42$ eV. The main

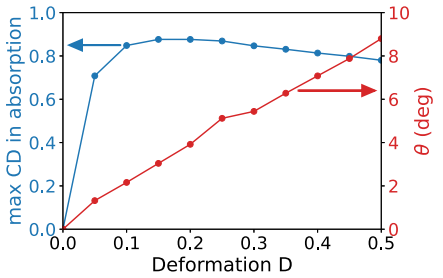

Figure 4. Summary results for maximum CD and angle theta of the maximum, as a function of the deformation, for a common semiaxis $r_1 = 200$ nm. The parameters are as shown in Figure 3.

conclusions are: (1) the maximum CD is nearly constant, it tends to zero only for very small deformations, and (2) the angle θ of the maximum CD increases almost linearly with the deformation. Such results are very similar to those of dielectric systems[46] and make us confident that, indeed, we are studying the properties of a BIC in a plasmonic system. The maximum value of CD can be related to the formation of polarization singularities, known as circularly polarized states, that spawn from the BIC along the x direction upon symmetry reduction.[38,39,45] The present metasurface design produces a well-identified BIC, which accordingly leads to a nearly optimal and robust CD at small values of the incidence angle.

The enhanced absorption CD associated with a BIC resonance is related to a substantial near-field effect that is produced by the metasurface with oval holes, as we show in the next section. As absorption and emission are reciprocal processes, preferential absorption of left or right CPL should translate into a highly circularly polarized emission. While these enhanced interactions occur close to the metasurface, understanding the emission characteristics in the far field becomes crucial for applications in which the emitted light propagates away from the metasurface. To this purpose, in

https://doi.org/10.1021/acsaom.4c00097
ACS Appl. Opt. Mater. 2024, 2, 825−833

Figure 5, we demonstrate extrinsic CD of PL emission from the metasurface with oval holes, adopting the same parameters

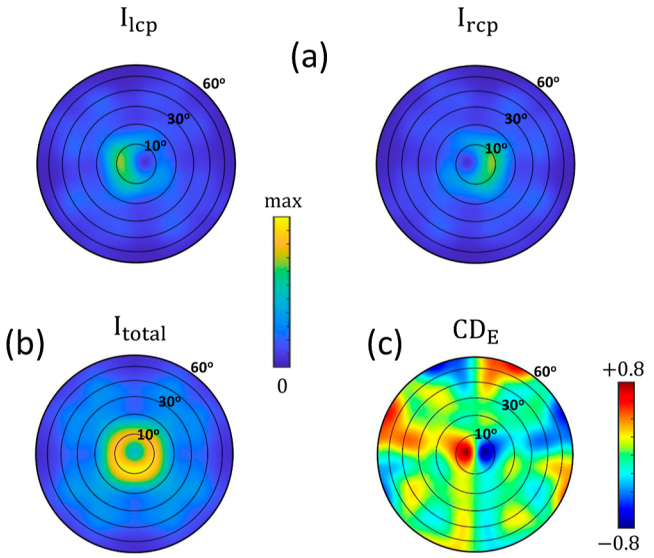

Figure 5. Polar plot of emission at the resonant energy of the q-BIC peak, E = 1.428 eV: (a) field intensities for left and right CPL, (b) total field intensity, and (c) far-field emission CD. The results are calculated for the metasurface of oval holes with r_1 = 200 nm, r_2 = 240 nm, and r_3 = 160 nm.

of Figure 2 (fourth column) and exciting the system with a random layer of dipoles at the resonant energy of the BIC mode. In Figure 5a, we see that the PL intensity is strongly enhanced at small emission angles, with a significant difference between the emission intensities I_{lcp} and I_{rcp} for left and right circular polarizations. LCP and RCP polarizations are directed to the opposite directions of the far-field hemisphere. Figure 5b shows the total emission intensity, whose far-field pattern reproduces the symmetry of the metasurface, with the presence of a vertical (yz) mirror plane. Finally, Figure 5c displays the emission CD defined in eq 2. A strong far-field emission CD is observed, reaching ±0.8 along the x orientation (azimuthal angles ϕ = 0 or 180°), which is the direction of maximum extrinsic chirality (note that high emission CD at large oblique incidence angles is not physically relevant due to the negligible emitted intensity and the definition in eq 2). Thus, the near-field absorption CD has a counterpart in the far-field emission CD when the emitted light couples to the BIC mode. We notice that the emission CD has not been specifically optimized and could be further enhanced by increasing the coupling efficiency or tailoring the symmetry breaking.

4. MODE PROFILES AND SYMMETRY ANALYSIS

In this section, we analyze the previous results from the point of view of the symmetry properties of the plasmonic metasurface. Specifically, we corroborate the identification of a q-BIC peak in comparison to the SPP peak. We start with the metasurface with the square lattice of circular holes, whose symmetry is described by the C_{4v} point group. This group has a two-dimensional (2D) irreducible representation with the symmetry of the in-plane dipole and four one-dimensional (1D) representations.[65,66] The 2D representation must correspond to the SPP peak, which indeed is a bright mode at a normal incidence. Each of the 1D representations is uncoupled to the far-field radiation at normal incidence and must, therefore, correspond to BICs.

In the following, we investigate the mode profiles by exciting the modes with dipole emitters with different configurations in the vicinity of the nanohole in the unit cell, and we calculate the electric and magnetic field components. At this point, we choose two different sets of four dipoles each, emitting at SPP resonance (E = 1.639 eV) and at BIC resonance (E = 1.428 eV), respectively. The field profiles are calculated in a 500 × 500 nm cell from a 2D monitor in the xy plane at a height of 5 nm above the glass (z = 5 nm). The detailed parameters of the two sets of dipoles and of the employed apodization procedure are listed in Section 6.

In Figure 6, we show the squared moduli of the fields for the two excitation energies and for the two sets of positions. It can be seen that the fields at the energy E = 1.639 eV of the SPP mode are more susceptible to variations in the dipole positions, leading to alterations in the electric and magnetic field distributions. Moreover, in one case (Pos1), the field profiles are not consistent with the symmetry of the metasurface: for example, $|\mathbf{E}|^2$ and $|\mathbf{H}|^2$ are not invariant under mirror reflections in the xz and yz planes. These features are consistent with the twofold degenerate nature of the SPP mode: indeed, such a mode can be excited in any linear combination of the two

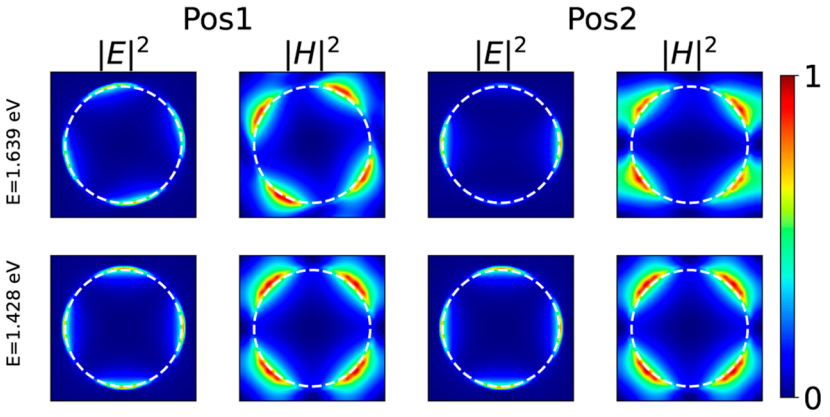

Figure 6. Full comparison of the electric and magnetic field modules squared at E = 1.639 eV (SPP mode) and E = 1.428 eV (BIC mode). The fields are calculated for a metasurface with circular holes, $r_1 = r_2 = r_3$ = 200 nm, by exciting with sets of dipoles in two positions (Pos1 and Pos2), as specified in the text. The field profiles are calculated in a 500 nm × 500 nm cell at a height of 5 nm above the glass (z = 5 nm).

https://doi.org/10.1021/acsaom.4c00097
ACS Appl. Opt. Mater. 2024, 2, 825−833

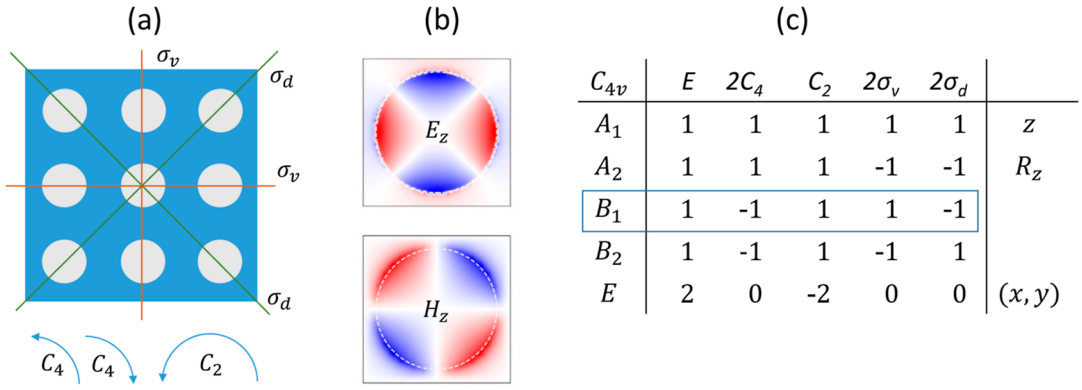

C_{4v}	E	$2C_4$	C_2	$2\sigma_v$	$2\sigma_d$	
A_1	1	1	1	1	1	z
A_2	1	1	1	-1	-1	R_z
B_1	1	-1	1	1	-1	
B_2	1	-1	1	-1	1	
E	2	0	-2	0	0	(x, y)

Figure 7. (a) Symmetries of the square lattice with circular holes, (b) E_z and H_z field profiles, and (c) character table of the point group C_{4v}. The mode profiles correspond to the irreducible representation B_1. The field profiles are calculated in a 500 × 500 nm cell at a height of 5 nm above the glass (z = 5 nm), as in Figure 6 for E = 1.428 eV.

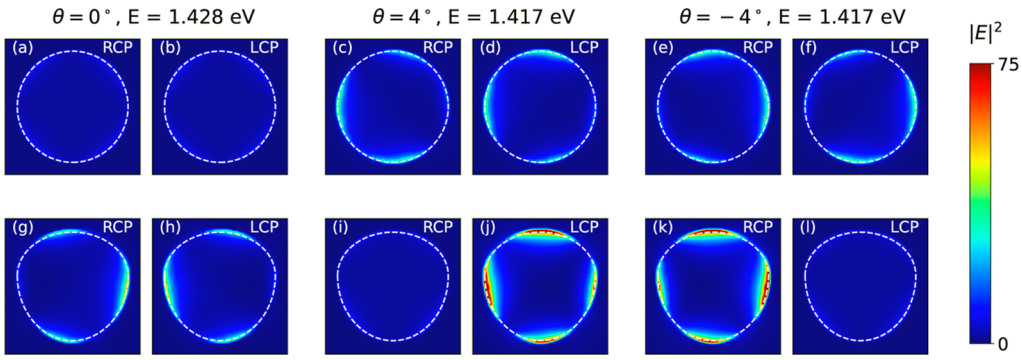

Figure 8. Electric field modulus squared for a metasurface with circular holes with $r_1 = r_2 = r_3$ = 200 nm (panels (a–f)) and for oval holes with r_1 = 200 nm, r_2 = 240 nm, and r_3 = 160 nm (panels (g–l)). The fields are calculated at normal incidence, energy E = 1.428 eV, and at $\theta = \pm 4°$, E = 1.417 eV, by exciting with either a right- or a left-circularly polarized plane wave. The incident field amplitude is E = 1 V m^{-1}, so that the plotted quantity is the intensity enhancement. Notice that the maximum intensity in panels (j and k) is $|E|^2$ = 160 V^2 m^{-2}. The field profiles are calculated in a 500 × 500 nm cell at a height z = 5 nm above the bottom of the metal. The hole profiles are indicated by thin white lines.

degenerate eigenmodes, depending on the exact conditions for the excitation. Thus, the field profiles at E = 1.639 eV confirm that we are exciting a twofold degenerate, dipole-active SPP eigenmode. In contrast, at the energy E = 1.428 eV, the squared moduli of the electric and magnetic fields do not change with different positions of the dipoles and are fully consistent with the C_{4v} symmetry of the square lattice. This gives firm evidence for the identification of the mode at E = 1.428 eV as a nondegenerate BIC. Indeed, when the mode is nondegenerate, its field profiles under resonant excitations are robust and not sensitive to variations in dipole locations.

In order to identify the symmetry properties of the BIC mode, in Figure 7, we examine the symmetry operations of the C_{4v} point group (Figure 7a) and their effect on the E_z, H_z field components (Figure 7b), comparing with the C_{4v} character table (Figure 7c). The effect of a symmetry operation $\hat{O}$ on a vector field $\mathbf{V}(\mathbf{r})$ is $\hat{O}\mathbf{V}(\mathbf{r}) = (\hat{O}\mathbf{V})(\hat{O}^{-1}\mathbf{r})$, i.e., the operator acts both on the vector components and on their spatial dependence. Keeping in mind that the electric field $\mathbf{E}$ is a normal (polar) vector, while the magnetic field $\mathbf{H}$ is a pseudo- (axial) vector, we can verify easily that both components transform according to the B_1 irreducible representation. For example, both E_z and H_z change sign under a C_4 rotation, while they do not change sign under a C_2 rotation. We now examine the effect of σ_v (mirror reflection in a vertical xz or yz plane) and σ_d (mirror reflection in a vertical plane rotated by 45° or 135° with respect to the xz plane). The spatial dependence of E_z is even under σ_v, while the spatial dependence of H_z is odd, but the H_z component of the pseudovector $\mathbf{H}$ is also odd under σ_v: thus, both components are eigenvectors of a σ_v operator with eigenvalue +1. A similar reasoning shows that both components are eigenvectors of a σ_d operator with an eigenvalue −1. We, therefore, conclude that the resonance at E = 1.428 eV originates from a plasmonic symmetry-protected BIC that belongs to the B_1 irreducible representation of point group C_{4v} for the case of circular holes. The symmetry breaking upon deformation of the circular holes into oval holes gives rise to a quasi-BIC with nearly maximal CD in the absorption spectra.

We further investigate the properties of the BIC mode by looking at the electric field enhancement for left and right CPL in the case of circular and oval holes metasurfaces, namely, circular hole in the Au film with $r_1 = r_2 = r_3$ = 200 nm and oval holes with r_1 = 200 nm, r_2 = 240 nm, and r_3 = 160 nm. In Figure 8, we show the squared modulus of the electric field in a xy cross section near the bottom of the Au film (z = 5 nm) for the energies of maximum absorption at BIC resonances at θ = 0° (E = 1.428 eV) and at $\theta = \pm 4°$ (E = 1.417 eV).

In the case of normal incidence (θ = 0°) and circular holes, the incoming radiation is uncoupled to the BIC mode, and there is no field enhancement. For oval holes, there is some enhancement, implying the excitation of a quasi-BIC mode, and we can see that fields for left and right circular

https://doi.org/10.1021/acsaom.4c00097
ACS Appl. Opt. Mater. 2024, 2, 825−833

polarizations are inverted under mirror reflection in the xz plane. On the other hand, at oblique incidence ($\theta = \pm 4°$), the field is weakly enhanced in the case of circular holes for left and right CPL, and the polarization is inverted under reflection in the xz plane, which is the only mirror plane in this situation.

In the case of oval holes at $\theta = 4°$, there is a marked difference between the local fields for the two circular polarizations: the quasi-BIC mode is uncoupled for right CPL, while it reaches a maximum value of $|E|^2 = 160\ V^2\ m^{-2}$ for left CPL (i.e., beyond the scale of the colorbar). Meanwhile, for $\theta = -4°$, the quasi-BIC mode is uncoupled for left CPL, while it reaches a maximum value of $|E|^2 = 160\ V^2\ m^{-2}$ for right CPL.

These results show that the quasi-BIC mode in the symmetry-broken metasurface is characterized by a strong enhancement of the local electric field, which is further increased at the angle $\theta = \pm 4°$, where the CD is maximized. In short, maximum extrinsic chirality spawn from the BIC is associated with a strong local field enhancement when a nearly ideal circularly polarized state is formed.

5. DISCUSSION AND CONCLUSIONS

The key findings of this study can be stated as follows. First, we predict nearly maximum CD in an Au metasurface with oval holes in the near-IR range. Second, we show that this phenomenon originates from a plasmonic BIC supported by the metasurface with circular holes, which evolves into a quasi-BIC upon the deformation of the holes. The quasi-BIC yields a strong chiral response at a finite value of the angle of incidence along the orientation that maximizes the symmetry-breaking effect. While the BIC itself is uncoupled to far-field radiation, identification of the BIC mode follows from several features: the optically active quasi-BIC (upon deformation and/or at non-normal incidence) is much narrower than the SPP mode; the field profiles do not depend on simulation conditions, indicating the occurrence of a nondegenerate resonant mode; finally, symmetry analysis of the field profiles for circular holes indicates an irreducible representation of the C_{4v} point group, which is dipole-forbidden at $k = 0$.

It is interesting to ask what are the conditions for a plasmonic BIC to occur in metasurfaces of the kind investigated here, namely, nanohole arrays supporting an EOT with SPP resonances. We believe that a crucial factor is to choose the geometrical parameters in such a way that *the BIC occurs on the low-energy side of the SPP peak*. The reason is that the SPP peak at normal incidence occurs at the energy of the folded SPP modes, whose dispersion is very close to the light line.[24] Thus, the frequency of the SPP mode at $\mathbf{k} = 0$ is also a diffraction cutoff. When the BIC mode is below the SPP mode, it is immune to diffraction, while when the mode falls above the SPP mode, it is subject to diffraction at high angles with a strong radiative broadening, thereby destroying the BIC nature.

Another interesting question that calls for further research is the limiting Q-factor of the quasi-BIC in the investigated metasurfaces and its relation to metallic losses, especially when changing the resonant wavelength. Indeed, the higher quality factor of the BIC modes compared to SPP modes paves the road toward plasmonic resonant applications, characterized by larger local field enhancement and narrower resonances. In the present work, we exploit a BIC in a plasmonic nanohole array in order to enhance CD in absorption. Thus, we do not need to leverage the coupling to lattice modes,[67,68] and the present structure is expected to preserve the advantage of the smaller footprint granted by plasmonic platforms. There is room for improving the Q-factor of BIC resonances by proper optimization. These advantages are especially relevant if we aim at operating the plasmonic metasurface sustaining BIC modes toward the infrared range of the spectrum at telecom wavelengths.

The absorption CD upon symmetry breaking of the circular holes raises up to a maximum value close to ± 1, it is almost independent of the size of the deformation, and the angle of maximum CD is proportional to the deformation. All these features are similar to those of dielectric metasurfaces,[38,39,46,69] and suggest that the present plasmonic structure supports topological singularities that evolve from a symmetry-protected BIC into circularly polarized states for any amount of symmetry breaking. Interestingly, this phenomenon occurs in a metal metasurface that is subject to dissipation, suggesting that these topological properties are nearly immune to ohmic losses. Further research is needed in order to elucidate the interplay between BICs (or, in general, topological singularities) and dissipative losses, which are typical of plasmonic materials. In any case, we can conclude that the concept of a plasmonic BIC with symmetry breaking is a promising route to achieve a strong chiral response in metallic metasurfaces, with a robust design that is almost independent of the magnitude of the deformation. We also underline the simplicity of the geometry, which can be produced by both advanced lithography techniques or with low-cost self-assembling shadow-sphere lithography.[30,70]

Another important finding of the present work is that the maximum value of the CD is found in both absorption and emission, and it is associated with a strong local field enhancement. Since the CD is maximum for a wide range of deformations, there is room for further optimization of the field enhancement. This can be exploited at the fundamental level to enhance all processes that rely on radiation−matter interaction, such as the control of chiral nonlinear optical effects and of chiral emission in active plasmonic metasurfaces. Also, it is promising for various applications that range from chiral sensing to quantum technologies. One could envisage, e.g., introducing local emitters in the nanoholes and investigating quantum correlations between pairs of circularly polarized photons emitted at $\pm\theta$. The results of the present work suggest that such a process would be nearly immune to losses, which is a crucial condition for the possible observation of true quantum correlations.

6. DETAILS ON THE METHOD

In this section, we provide the parameters of the dipole configurations that we used in the study to obtain Figure 6. These dipoles were positioned in the vicinity of the nanohole array at height $z = 0$ and emitting at SPP and BIC resonances. We set the phase of each dipole to 0°. The two sets of parameters are shown in Table 1 and include the in-plane positions (x, y) as well as the orientations given by the polar and azimuthal angles θ, ϕ.

Moreover, we collected the data from a 2D monitor in the xy plane, and this monitor was positioned at $z = 5$ nm above the glass substrate. We set the apodization of the monitor at the start to exclude the effects that occur at the end of the simulation. The apodization in the 2D monitor is centered at 300 fs with a time width of 50 fs, allowing it to filter out the

https://doi.org/10.1021/acsaom.4c00097
ACS Appl. Opt. Mater. 2024, 2, 825−833

Table 1. Dipoles Characterization at $z = 0$

	position1			position2		
	θ (deg)	ϕ (deg)	(x, y) nm	θ (deg)	ϕ (deg)	(x, y) nm
dipole1	45	0	(172, 100)	45	0	(−90, 100)
dipole2	33	0	(−180, 0)	33	0	(120, 50)
dipole3	0	0	(−150, −130)	0	0	(30, −150)
dipole4	45	22.2	(0, 0)	45	22.2	(30, −150)

field directly radiated by the dipole, leaving only the field of the resonance.

AUTHOR INFORMATION

Corresponding Author

Hanan Ali − *Department of Physics, University of Pavia, 27100 Pavia, Italy;* orcid.org/0009-0007-6316-9814; Email: hanan.ali01@universitadipavia.it

Authors

Simone Zanotti − *Department of Physics, University of Pavia, 27100 Pavia, Italy;* orcid.org/0000-0003-1515-7011

Giovanni Pellegrini − *Department of Physics, University of Pavia, 27100 Pavia, Italy;* orcid.org/0000-0003-0105-3449

Emilija Petronijevic − *Department S.B.A.I., Sapienza Università di Roma, I-00161 Rome, Italy;* orcid.org/0000-0003-1034-3843

Lucio Claudio Andreani − *Department of Physics, University of Pavia, 27100 Pavia, Italy;* orcid.org/0000-0003-4926-1749

Complete contact information is available at: https://pubs.acs.org/10.1021/acsaom.4c00097

Notes

The authors declare no competing financial interest.

ACKNOWLEDGMENTS

The authors acknowledge financial support from PNRR MUR project PE0000023-NQSTI.

REFERENCES

(1) Ebbesen, T.; Lezec, H.; Ghaemi, H.; Thio, T.; Wolff, P. Extraordinary optical transmission through sub-wavelength hole arrays. *Nature* **1998**, *391*, 667−669.

(2) García de Abajo, F. J. Colloquium: light scattering by particle and hole arrays. *Rev. Mod. Phys.* **2007**, *79*, 1267−1290.

(3) Barnes, W.; Dereux, A.; Ebbesen, T. Surface plasmon subwavelength optics. *Nature* **2003**, *424*, 824−830.

(4) Maier, S. A. *Plasmonics: Fundamentals and Applications*; Springer, 2007.

(5) Liu, H.; Lalanne, P. Microscopic theory of the extraordinary optical transmission. *Nature* **2008**, *452*, 728−731.

(6) Meinzer, N.; Barnes, W.; Hooper, I. Plasmonic meta-atoms and metasurfaces. *Nat. Photonics* **2014**, *8*, 889−898.

(7) Yue, W.; Wang, Z.; Yang, Y.; Li, J.; Wu, Y.; Chen, L.; Ooi, B.; Wang, X.; Zhang, X.-x. Enhanced extraordinary optical transmission (EOT) through arrays of bridged nanohole pairs and their sensing applications. *Nanoscale* **2014**, *6*, 7917−7923.

(8) Blanchard-Dionne, A.-P.; Meunier, M. Sensing with periodic nanohole arrays. *Adv. Opt. Photon* **2017**, *9*, 891−940.

(9) Wang, Z.; Chen, J.; Khan, S.; Li, F.; Shen, J.; Duan, Q.; Liu, X.; Zhu, J. Plasmonic Metasurfaces for Medical Diagnosis Applications: A Review. *Sensors* **2021**, *22*, 133.

(10) Solomon, M. L.; Saleh, A. A. E.; Poulikakos, L. V.; Abendroth, J. M.; Tadesse, L. F.; Dionne, J. A. Nanophotonic Platforms for Chiral Sensing and Separation. *Acc. Chem. Res.* **2020**, *53*, 588−598.

(11) Altug, H.; Oh, S.-H.; Maier, S. A.; Homola, J. Advances and applications of nanophotonic biosensors. *Nat. Nanotechnol.* **2022**, *17*, 5−16.

(12) Kelvin, L. *The Molecular Tactics of a Crystal*; Clarendon, 1894.

(13) Barron, L. D. *Molecular Light Scattering and Optical Activity*, 2nd ed.; Cambridge University, 2009.

(14) Chuong, P. H.; Nguyen, L. A.; He, H. Chiral drugs: an overview. *Int. J. Biomed. Sci.* **2006**, *2*, 85−100.

(15) Nesterov, M.; Yin, X.; Schäferling, M.; Giessen, H.; Weiss, T. The Role of Plasmon-Generated Near Fields for Enhanced Circular Dichroism Spectroscopy. *ACS Photonics* **2016**, *3*, 578−583.

(16) Schaeferling, M. *Chiral Nanophotonics - Chiral Optical Properties of Plasmonic Systems*; Springer Series in Optical Sciences; Springer: Switzerland, 2017; Vol. *205*.

(17) Collins, J.; Kuppe, C.; Hooper, D.; Sibilia, C.; Centini, M.; Valev, V. Chirality and Chiroptical Effects in Metal Nanostructures: Fundamentals and Current Trends. *Adv. Optical Mater.* **2017**, *5*, 1700182.

(18) Wang, X.; Tang, Z. Circular Dichroism Studies on Plasmonic Nanostructures. *Small* **2017**, *13*, 1601115.

(19) Mun, J.; Kim, M.; Yang, Y.; Badloe, T.; Ni, J.; Chen, Y.; Qiu, C.; Rho, J. Electromagnetic chirality: from fundamentals to nontraditional chiroptical phenomena. *Light: Sci. Appl.* **2020**, *9*, 139.

(20) Petronijevic, E.; Belardini, A.; Leahu, G.; Cesca, T.; Scian, C.; Mattei, G.; Sibilia, C. Circular Dichroism in Low-Cost Plasmonics: 2D Arrays of Nanoholes in Silver. *Appl. Sci.* **2020**, *10*, 1316.

(21) Petronijevic, E.; Ali, H.; Zaric, N.; Belardini, A.; Leahu, G.; Cesca, T.; Mattei, G.; Andreani, L.; Sibilia, C. Chiral effects in low-cost plasmonic arrays of elliptic nanoholes. *Opt. Quantum Electron.* **2020**, *52*, 176.

(22) Serrera, G.; González-Colsa, J.; Giannini, V.; Saiz, J. M.; Albella, P. Enhanced optical chirality with directional emission of Surface Plasmon Polaritons for chiral sensing applications. *J. Quant. Spectrosc. Radiat. Transfer* **2022**, *284*, 108166.

(23) Lininger, A.; Palermo, G.; Guglielmelli, A.; Nicoletta, G.; Goel, M.; Hinczewski, M.; Strangi, G. Chirality in Light−Matter Interaction. *Adv. Mater.* **2022**, *35*, 2107325.

(24) Ali, H.; Petronijevic, E.; Pellegrini, G.; Sibilia, C.; Andreani, L. C. Circular dichroism in a plasmonic array of elliptical nanoholes with square lattice. *Opt. Express* **2023**, *31*, 14196−14211.

(25) Höflich, K.; Feichtner, T.; Hansjürgen, E.; Haverkamp, C.; Kollmann, H.; Lienau, C.; Silies, M. Resonant behavior of a single plasmonic helix. *Optica* **2019**, *6*, 1098−1105.

(26) Kan, Y.; Andersen, S. K. H.; Ding, F.; Kumar, S.; Zhao, C.; Bozhevolnyi, S. I. Metasurface-Enabled Generation of Circularly Polarized Single Photons. *Adv. Mater.* **2020**, *32*, 1907832.

(27) Gilroy, C.; Koyroytsaltis-McQuire, D. J. P.; Gadegaard, N.; Karimullah, A. S.; Kadodwala, M. Superchiral hot-spots in "real" chiral plasmonic structures. *Mater. Adv.* **2022**, *3*, 346−354.

(28) Plum, E.; Fedotov, V. A.; Zheludev, N. I. Extrinsic electromagnetic chirality in metamaterials. *J. Opt. A: Pure Appl. Opt.* **2009**, *11*, 074009.

(29) Belardini, A.; Centini, M.; Leahu, G.; Hooper, D. C.; Li Voti, R.; Fazio, E.; Haus, J. W.; Sarangan, A.; Valev, V. K.; Sibilia, C. Chiral light intrinsically couples to extrinsic/pseudo-chiral metasurfaces made of tilted gold nanowires. *Sci. Rep.* **2016**, *6*, 31796.

(30) Petronijević, E.; Leahu, G.; Li Voti, R.; Belardini, A.; Scian, C.; Michieli, N.; Cesca, T.; Mattei, G.; Sibilia, C. Photo-acoustic detection of chirality in metal-polystyrene metasurfaces. *Appl. Phys. Lett.* **2019**, *114*, 053101.

(31) Leahu, G.; Petronijevic, E.; Li Voti, R.; Belardini, A.; Cesca, T.; Mattei, G.; Sibilia, C. Diffracted Beams from Metasurfaces: High

Chiral Detectivity by Photothermal Deflection Technique. *Adv. Opt. Mater.* **2021**, *9*, 2100670.
(32) Petronijevic, E.; Belardini, A.; Cesca, T.; Scian, C.; Mattei, G.; Sibilia, C. Rich Near-Infrared Chiral Behavior in Diffractive Metasurfaces. *Phys. Rev. Appl.* **2021**, *16*, 014003.
(33) Marinica, D. C.; Borisov, A. G.; Shabanov, S. V. Bound States in the Continuum in Photonics. *Phys. Rev. Lett.* **2008**, *100*, 183902.
(34) Plotnik, Y.; Peleg, O.; Dreisow, F.; Heinrich, M.; Nolte, S.; Szameit, A.; Segev, M. Experimental Observation of Optical Bound States in the Continuum. *Phys. Rev. Lett.* **2011**, *107*, 183901.
(35) Hsu, C. W.; Zhen, B.; Stone, A. D.; Joannopoulos, J. D.; Soljačić, M. Bound states in the continuum. *Nat. Rev. Mater.* **2016**, *1*, 16048.
(36) Kang, M.; Liu, T.; Chan, C. T.; Xiao, M. Applications of bound states in the continuum in photonics. *Nat. Rev. Phys.* **2023**, *5*, 659−678.
(37) Zhen, B.; Hsu, C. W.; Lu, L.; Stone, A. D.; Soljačić, M. Topological Nature of Optical Bound States in the Continuum. *Phys. Rev. Lett.* **2014**, *113*, 257401.
(38) Liu, W.; Wang, B.; Zhang, Y.; Wang, J.; Zhao, M.; Guan, F.; Liu, X.; Shi, L.; Zi, J. Circularly Polarized States Spawning from Bound States in the Continuum. *Phys. Rev. Lett.* **2019**, *123*, 116104.
(39) Yoda, T.; Notomi, M. Generation and Annihilation of Topologically Protected Bound States in the Continuum and Circularly Polarized States by Symmetry Breaking. *Phys. Rev. Lett.* **2020**, *125*, 053902.
(40) Gorkunov, M. V.; Antonov, A. A.; Tuz, V. R.; Kupriianov, A. S.; Kivshar, Y. S. Bound States in the Continuum Underpin Near-Lossless Maximum Chirality in Dielectric Metasurfaces. *Adv. Opt. Mater.* **2021**, *9*, 2100797.
(41) Liu, W.; Liu, W.; Shi, L.; Kivshar, Y. Topological polarization singularities in metaphotonics. *Nanophotonics* **2021**, *10*, 1469−1486.
(42) Wu, J.; Xu, X.; Su, X.; Zhao, S.; Wu, C.; Sun, Y.; Li, Y.; Wu, F.; Guo, Z.; Jiang, H.; Chen, H. Observation of Giant Extrinsic Chirality Empowered by Quasi-Bound States in the Continuum. *Phys. Rev. Appl.* **2021**, *16*, 064018.
(43) Chen, W.; Yang, Q.; Chen, Y.; Liu, W. Extremize Optical Chiralities through Polarization Singularities. *Phys. Rev. Lett.* **2021**, *126*, 253901.
(44) Zhang, X.; Liu, Y.; Han, J.; Kivshar, Y.; Song, Q. Chiral emission from resonant metasurfaces. *Science* **2022**, *377*, 1215−1218.
(45) Wang, X.; Wang, J.; Zhao, X.; Shi, L.; Zi, J. Realizing Tunable Evolution of Bound States in the Continuum and Circularly Polarized Points by Symmetry Breaking. *ACS Photonics* **2023**, *10*, 2316−2322.
(46) Zagaglia, L.; Zanotti, S.; Minkov, M.; Liscidini, M.; Gerace, D.; Andreani, L. C. Polarization states and far-field optical properties in dielectric photonic crystal slabs. *Opt. Lett.* **2023**, *48*, 5017−5020.
(47) Azzam, S. I.; Shalaev, V. M.; Boltasseva, A.; Kildishev, A. V. Formation of Bound States in the Continuum in Hybrid Plasmonic-Photonic Systems. *Phys. Rev. Lett.* **2018**, *121*, 253901.
(48) Pavlov, A.; Zabkov, I.; Klimov, V. Lasing threshold of the bound states in the continuum in the plasmonic lattices. *Opt. Express* **2018**, *26*, 28948−28962.
(49) Liang, Y.; Koshelev, K.; Zhang, F.; Lin, H.; Lin, S.; Wu, J.; Jia, B.; Kivshar, Y. Bound States in the Continuum in Anisotropic Plasmonic Metasurfaces. *Nano Lett.* **2020**, *20*, 6351−6356.
(50) Seo, I. C.; Kim, S.; Woo, B. H.; Chung, I.-S.; Jun, Y. C. Fourier-plane investigation of plasmonic bound states in the continuum and molecular emission coupling. *Nanophotonics* **2020**, *9*, 4565−4577.
(51) Sun, S.; Ding, Y.; Li, H.; Hu, P.; Cheng, C.-W.; Sang, Y.; Cao, F.; Hu, Y.; Alu, A.; Liu, D.; Wang, Z.; Gwo, S.; Han, D.; Shi, J. Tunable plasmonic bound states in the continuum in the visible range. *Phys. Rev. B* **2021**, *103*, 045416.
(52) Aigner, A.; Tittl, A.; Wang, J.; Weber, T.; Kivshar, Y.; Maier, S. A.; Ren, H. Plasmonic bound states in the continuum to tailor light-matter coupling. *Sci. Adv.* **2022**, *8*, No. eadd4816.
(53) Shen, Z.; Fang, X.; Li, S.; Yin, W.; Zhang, L.; Chen, X. Terahertz spin-selective perfect absorption enabled by quasi-bound states in the continuum. *Opt. Lett.* **2022**, *47*, 505−508.
(54) Trinh, Q. T.; Nguyen, S. K.; Nguyen, D. H.; Tran, G. K.; Le, V. H.; Nguyen, H.-S.; Le-Van, Q. Coexistence of surface lattice resonances and bound states in the continuum in a plasmonic lattice. *Opt. Lett.* **2022**, *47*, 1510−1513.
(55) Wang, J.; Weber, T.; Aigner, A.; Maier, S. A.; Tittl, A. Mirror-Coupled Plasmonic Bound States in the Continuum for Tunable Perfect Absorption. *Laser Photonics Rev.* **2023**, *17*, 2300294.
(56) Wang, Z.; Liang, Y.; Qu, J.; Chen, M. K.; Cui, M.; Cheng, Z.; Zhang, J.; Yao, J.; Chen, S.; Tsai, D. P.; Yu, C. Plasmonic bound states in the continuum for unpolarized weak spatially coherent light. *Photonics Res.* **2023**, *11*, 260−269.
(57) Tang, Y.; Liang, Y.; Yao, J.; Chen, M. K.; Lin, S.; Wang, Z.; Zhang, J.; Huang, X. G.; Yu, C.; Tsai, D. P. Chiral Bound States in the Continuum in Plasmonic Metasurfaces. *Laser Photonics Rev.* **2023**, *17*, 2200597.
(58) Liu, D.; Ren, Y.; Huo, Y.; Cai, Y.; Ning, T. Second harmonic generation in plasmonic metasurfaces enhanced by symmetry-protected dual bound states in the continuum. *Opt. Express* **2023**, *31*, 23127−23139.
(59) Dossou, K.; Botten, L.; Asatryan, A.; Sturmberg, B.; Byrne, M.; Poulton, C.; McPhedran, R.; de Sterke, C. M. Modal formulation for diffraction by absorbing photonic crystal slabs. *J. Opt. Soc. Am. A* **2012**, *29*, 817−831.
(60) Sturmberg, B.; Dossou, K.; Lawrence, F. J.; Poulton, C. G.; McPhedran, R. C.; Martijn de Sterke, C.; Botten, L. C. EMUstack: An open source route to insightful electromagnetic computation via the Bloch mode scattering matrix method. *Comput. Phys. Commun.* **2016**, *202*, 276−286.
(61) Liang, B.; Bai, M.; Ma, H.; Ou, N.; Miao, J. Wideband Analysis of Periodic Structures at Oblique Incidence by Material Independent FDTD Algorithm. *IEEE Trans. Antennas Propag.* **2014**, *62*, 354−360.
(62) *CRC Handbook of Chemistry and Physics*, 103rd ed.; Rumble, J., Ed.; CRC, 2022.
(63) Maoz, B. M.; Ben Moshe, A.; Vestler, D.; Bar-Elli, O.; Markovich, G. Chiroptical Effects in Planar Achiral Plasmonic Oriented Nanohole Arrays. *Nano Lett.* **2012**, *12*, 2357−2361.
(64) Ren, S.; Liu, C.; Xu, K.; Jiang, N.; Hu, F.; Tan, P.-H.; Zheng, H.; Xu, X.; Shen, C.; Zhang, J. Azimuth-Resolved Circular Dichroism of Metamaterials. *J. Phys. Chem. Lett.* **2022**, *13*, 1697−1704.
(65) Koster, G. F.; Dimmock, J. O.; Wheeler, R. G.; Statz, H. *The Properties of the Thirty-Two Point Groups*; MIT Press: Cambridge, MA, 1963.
(66) Sakoda, K. *Optical Properties of Photonic Crystals*, 2nd ed.; Springer: Berlin, 2005.
(67) Bin-Alam, M. S.; Reshef, O.; Mamchur, Y.; Alam, M. Z.; Carlow, G.; Upham, J.; Sullivan, B. T.; Ménard, J. M.; Huttunen, M. J.; Boyd, R. W.; Dolgaleva, K. Ultra-high-Q resonances in plasmonic metasurfaces. *Nat. Commun.* **2021**, *12*, 974.
(68) Cerdán, L.; Zundel, L.; Manjavacas, A. Chiral Lattice Resonances in 2.5-Dimensional Periodic Arrays with Achiral Unit Cells. *ACS Photonics* **2023**, *10*, 1925−1935.
(69) Liu, W.-Z.; Shi, L.; Chan, C.-T.; Zi, J. Momentum-space polarization fields in two-dimensional photonic-crystal slabs: Physics and applications. *Chin. Phys. B* **2022**, *31*, 104211.
(70) Ai, B.; Luong, H. M.; Zhao, Y. Chiral nanohole arrays. *Nanoscale* **2020**, *12*, 2479−2491.

https://doi.org/10.1021/acsaom.4c00097
ACS Appl. Opt. Mater. 2024, 2, 825−833